Article

Cell Systems

Stochastic Self-Assembly of ParB Proteins Builds the Bacterial DNA Segregation Apparatus

Graphical Abstract

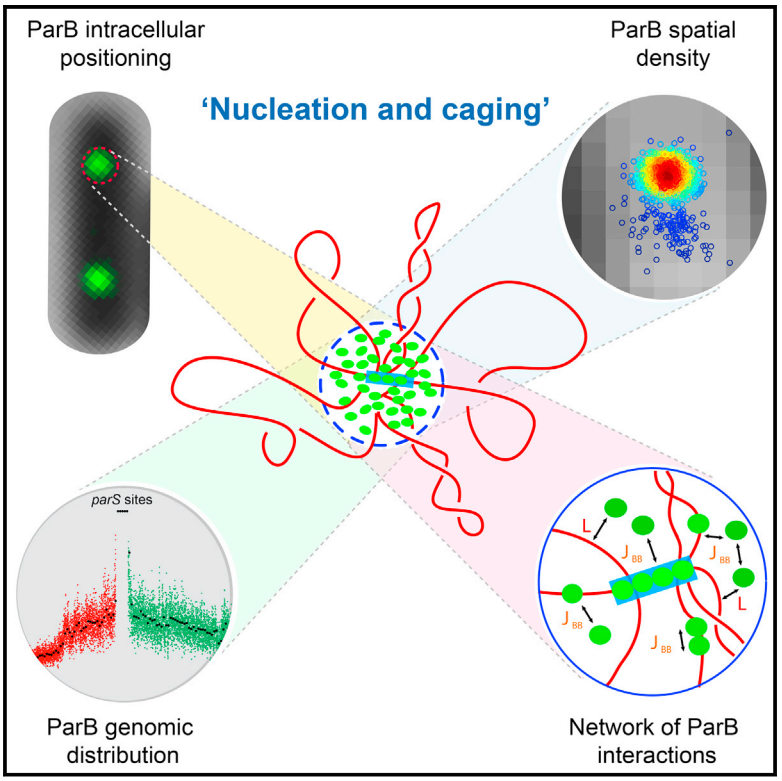

Authors

Aurore Sanchez, Diego I. Cattoni, Jean-Charles Walter, ..., Andrea Parmeggiani, Marcelo Nollmann, Jean-Yves Bouet

Correspondence

jean-yves.bouet@ibcg.biotoul.fr

In Brief

Sanchez et al. use super-resolution microscopy, modeling, and classical biochemistry to investigate the assembly mechanism of the bacterial partition complex ParB on centromeric DNA. They propose a new model, termed nucleation and caging, for ParB self-assembly; it involves stochastic binding and active confinement of ParBs on DNA near the centromere.

Highlights

- From PALM, more than 90% of ParB proteins are actively confined at *parS* sites
- A network of three synergistic, independent interactions drives ParB confinement
- Stochastic binding to non-specific DNA organizes the partition complex in space
- A nucleation and caging mechanism describes the dynamic assembly near *parS* sites

Accession Numbers

GSE67869

Sanchez et al., 2015, Cell Systems *1*, 163–173
August 26, 2015
http://dx.doi.org/10.1016/j.cels.2015.07.013

CellPress

Cell Systems
Article

Stochastic Self-Assembly of ParB Proteins Builds the Bacterial DNA Segregation Apparatus

Aurore Sanchez,[1,2] Diego I. Cattoni,[3] Jean-Charles Walter,[1,2,4] Jérôme Rech,[1,2] Andrea Parmeggiani,[4,5] Marcelo Nollmann,[3] and Jean-Yves Bouet[1,2,*]
[1]Laboratoire de Microbiologie et Génétique Moléculaires, Centre National de la Recherche Scientifique, 31062 Toulouse, France
[2]Laboratoire de Microbiologie et Génétique Moléculaires, Université de Toulouse 3, 31062 Toulouse, France
[3]Centre de Biochimie Structurale, Institut National de la Santé et la Recherche Médicale U554, Centre National de la Recherche Scientifique UMR5048, Université de Montpellier, 34090 Montpellier, France
[4]Laboratoire Charles Coulomb, UMR5221 CNRS-Université de Montpellier, 34095 Montpellier, France
[5]Dynamique des Interactions Membranaires Normales et Pathologiques, UMR 5235 CNRS-Université de Montpellier, 34095 Montpellier, France
*Correspondence: jean-yves.bouet@ibcg.biotoul.fr
http://dx.doi.org/10.1016/j.cels.2015.07.013

SUMMARY

Many canonical processes in molecular biology rely on the dynamic assembly of higher-order nucleoprotein complexes. In bacteria, the assembly mechanism of ParABS, the nucleoprotein super-complex that actively segregates the bacterial chromosome and many plasmids, remains elusive. We combined super-resolution microscopy, quantitative genome-wide surveys, biochemistry, and mathematical modeling to investigate the assembly of ParB at the centromere-like sequences *parS*. We found that nearly all ParB molecules are actively confined around *parS* by a network of synergistic protein-protein and protein-DNA interactions. Interrogation of the empirically determined, high-resolution ParB genomic distribution with modeling suggests that instead of binding only to specific sequences and subsequently spreading, ParB binds stochastically around *parS* over long distances. We propose a new model for the formation of the ParABS partition complex based on nucleation and caging: ParB forms a dynamic lattice with the DNA around *parS*. This assembly model and approach to characterizing large-scale, dynamic interactions between macromolecules may be generalizable to many unrelated machineries that self-assemble in superstructures.

INTRODUCTION

The function of many cellular structures is intrinsic to their cellular localization and mechanism of assembly. A striking example of such an assembly is the DNA segregation apparatus. In most bacteria, active DNA segregation is driven by three-component partition machineries (reviewed in Salje, 2010). Type I partition systems, which are the most prevalent in low copy-number plasmids and the only type present on bacterial chromosomes, are generically called ParABS. The ParB family members specifically recognize DNA sequences (*parS*) and assemble a higher-order nucleoprotein complex, named the partition complex. Bacterial *parS* sites are cytologically different from eukaryotic centromeres but are functionally equivalent: they assemble multi-protein structures that ensure active bacterial DNA segregation. They are hereafter called *parS* centromeres.

After centromere replication, the formation of the partition complex promotes segregation of plasmids or chromosomes to daughter cells by interacting with its cognate protein, ParA (Bouet and Funnell, 1999; for a review, see Vecchiarelli et al., 2012). In type II and III partition systems, the partition complex architecture is structurally well defined and displays DNA-protein filaments with centromere sequences wrapped around a helical scaffold made of centromere-binding proteins (Aylett and Löwe, 2012; Møller-Jensen et al., 2007; Salje and Löwe, 2008; Schumacher et al., 2007). In contrast, in type I partition systems, the overall organization and architecture of partition complexes are not known. The determination of the partition complex scaffold and assembly mechanism is key to decipher its precise role in the regulation and dynamics of bacterial chromosome segregation.

ParB proteins share a general organization with three functional modules: a N-terminal domain that interacts with ParA (Surtees and Funnell, 1999) and stimulates its ATP hydrolysis (Ah-Seng et al., 2009), a central domain for binding to *parS* and non-specific DNA (nsDNA) binding (Sanchez et al., 2013), and a C-terminal dimerization domain (Surtees and Funnell, 1999). The primary binding of ParB to *parS* is well characterized (Bouet et al., 2000; Funnell, 1991; Lin and Grossman, 1998; Pillet et al., 2011; Schumacher and Funnell, 2005). Initially, the proposed assembly of a higher-order structure on centromeres was based on measurements of F plasmid supercoiling (Biek and Shi, 1994) and gene silencing in the vicinity of *parS* upon ParB binding (Lynch and Wang, 1995). At physiological levels, ParB binds over a large region flanking *parS* sites on plasmids, up to 12 kilobases (kb; Rodionov et al., 1999) and chromosomes (more than 10 kb; Breier and Grossman, 2007). Two models were proposed to describe the assembly of partition complexes involved in active DNA segregation. The lateral spreading model, also called the ParB filament model (Figure 1A), proposed that nearest-neighbor interactions between ParB sub-units lead to

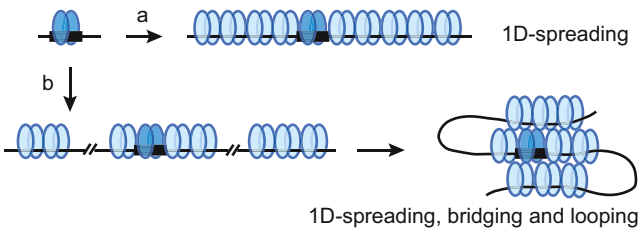

Figure 1. Current Models for ParB Spreading and Partition Complex Assembly

Schematic representation of the main currently proposed mechanisms for the assembly of partition complexes. The ParB dimer (dark blue ovoids) binds specifically to the *parS* centromere site (black rectangle).

(A) 1D spreading. ParB dimers propagate by nearest-neighbor interactions in 1D following the DNA track (black line) and form filaments away from *parS* in both directions.

(B) 1D polymerization, bridging, and looping. ParB dimers form (short) 1D filaments on *parS* and on nsDNA by nearest-neighbor interactions. By bridging together, these patches of ParB induce the formation of DNA loops.

one-dimensional (1D) spreading of ParB from *parS* sites (Murray et al., 2006; Rodionov et al., 1999). More recently, the spreading and bridging model (Figure 1B) proposed that in addition to 1D spreading, ParB-mediated 3D bridging and looping allows ParB to cover large distances away from *parS* (Broedersz et al., 2014; Graham et al., 2014; Taylor et al., 2015). However, several lines of evidence do not conform to these models. In particular, the latter model relies on studies analyzing ParB binding to flow-stretched DNA in which no effect of the presence of *parS* was detected. This contradicts in vivo data showing that the absence of *parS* sites prevents the formation of clusters (Erdmann et al., 1999).

To shed light on the assembly mechanism of type I partition complexes, we used the archetypical type I partition system of the F plasmid SopABC (hereafter referred as $ParABS_F$) and applied a unique combination of in vivo and in vitro approaches. Super-resolution microscopy was used to determine the subcellular localization of partition complexes with nanometer precision and quantify, at the single-molecule level, the relative proportions of $ParB_F$ in and out of these complexes across time. Genome-wide methods were used to obtain the distribution of $ParB_F$ binding along DNA at nucleotide resolution, while biochemical methods provided insight into the molecular mechanism of partition complex formation. In addition, we provide a theoretical framework that synthesizes our findings into a single new model in which a network of stochastic, dynamic interactions of $ParB_F$ leads to the partition complex assembly. Our model has major implications for the mechanism of active DNA segregation in bacteria and may be generalizable to all ParBs involved in active DNA segregation and similar machineries in prokaryotes and eukaryotes.

RESULTS

Most of the $ParB_F$ Cellular Pool Dynamically Localizes to Diffraction-Limited Partition Complexes

Partition complexes are formed by the specific binding of ParB to *parS*, whereas their cellular localization is dictated by the ParA ATPase. Interestingly, $ParB_F$ is present in a large excess (~800 dimers) with respect to the number of centromeres in the cell (~200 dimers per $parS_F$ sequence; Adachi et al., 2006; Bouet et al., 2005). This large excess of $ParB_F$ may be required for maintenance of the structural cohesion of partition complexes. Alternatively, this excess may be involved in the oscillation behavior of ParA, leading to the transport of partition complexes. To discern between these possibilities, we turned to single-molecule localization microscopy (SMLM), a method that allows for the detection and localization of individual molecules at the nanometer scale (Betzig et al., 2006; Hess et al., 2006; Rust et al., 2006).

First, we investigated the cellular localization of single $ParB_F$ molecules in live cells. We tagged $ParB_F$ with a monomeric photo-activatable fluorescent protein (mEos2) and employed a microfluidics-coupled, PALM (photo-activated localization microscopy) microscope to perform automatic, high-throughput, super-resolution detection and analysis (Cattoni et al., 2013; Fiche et al., 2013) of $ParB_F$-mEos2 localization in live cells. As a control, an equivalent fusion of $ParB_F$ with monomeric Venus was constructed ($ParB_F$-mVenus). In experimental conditions identical to those used for SMLM, mini-F plasmids were fully stable, ParA oscillation behavior was unperturbed, and expression levels of tagged ParB were comparable to wild-type ParB levels (Figures S1B–S1E).

Epi-fluorescence visualization of non-photo-activated $ParB_F$-mEos2 resulted in a similar localization pattern to that observed for $ParB_F$-mVenus (Figures 2A, 2B, and S1D). Foci detected by conventional epi-fluorescence imaging and SMLM were positioned at midcell for cells with a single cluster and at the quarter-cell position for cells with two clusters (Figure 2D). To investigate the spatial distribution of $ParB_F$, single-molecule localizations were displayed in a pointillist representation (Figures 2Ei, S2Ai, S2Bi, and S2Ci). The majority of molecules were found at the locations of the foci, and few molecules were detected outside the foci (i.e., freely diffusing $ParB_F$). To further study the internal organization of the foci, we quantified the spatial density of $ParB_F$ molecules employing an exploratory radius of 100 nm (Figures 2Eii, S2Aii, S2Bii, and S2Cii; see Experimental Procedures). This analysis confirmed that the majority of $ParB_F$ molecules are positioned within a small central region of the partition complex. To detect whether the partition complexes were dynamic, we split the total acquisition time into three time windows and represented the localization density maps for each time window (Figures 2Eiii, S2Aiii, S2Biii, and S2Ciii; the first time window is shown in red, the second is in green, and the last is in blue). Most of the foci show several colors, suggesting that despite being restricted to a small spatial region, partition complexes display dynamic behavior on the second or minute scale. This dynamic behavior suggests that ParB-*parS* partition complexes have a physical size that is smaller than that assumed from conventional microscopy techniques. The observed size of $ParB_F$ clusters represents confinement zones of ParB whose size is determined by the combination of the true size of the assembled partition complexes and its inherent dynamics.

To further quantify the cellular distribution of individual $ParB_F$-mEos2 molecules and the confinement zone sizes, single-molecule localization events were automatically clustered (Cattoni et al., 2013). To ensure that clusters were not associated with

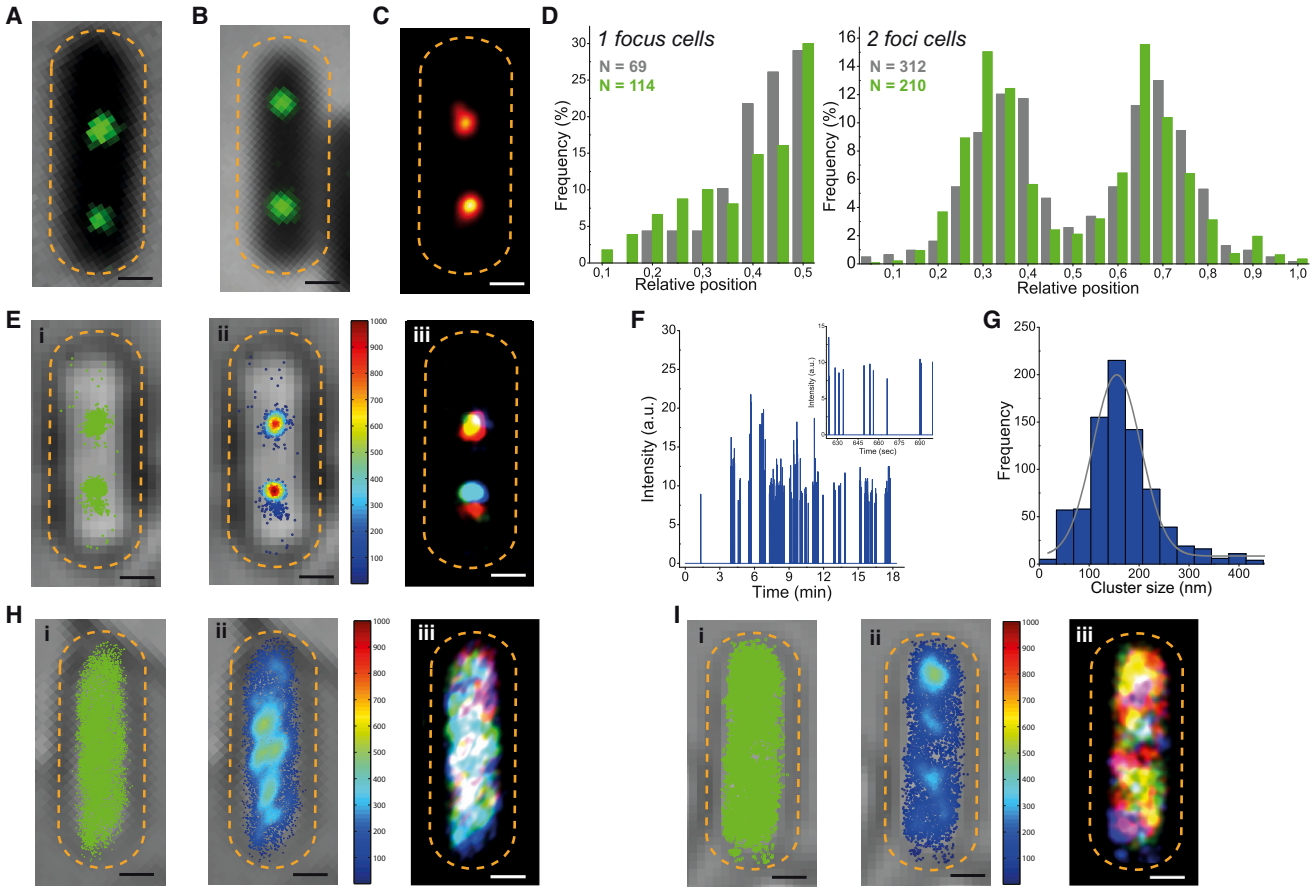

Figure 2. ParB$_F$ Assembles into Complexes Smaller Than 75 nm in Radius by Interacting Specifically with *parS*$_F$

(A and B) Conventional epi-fluorescence images of *E. coli* cells, in which ParB$_F$ (green) tagged with mVenus (A) or photo-activatable mEos2 (B) assemble in diffraction-limited foci.

(C) Individual ParB$_F$ proteins, which were detected by PALM microscopy and rendered into a super-resolution image, where the diameter of spots reflects the precision of the localization of each single-molecule event.

(D) Intracellular positioning of ParB$_F$-mVenus (gray columns) and ParB$_F$-mEos2 (green columns) from the cell edge for one focus (left panel) and two foci (right panel) containing cells as a function of the relative cell length. The number (N) of cells measured is indicated on each panel.

(E) The majority of ParB$_F$ assembled into dynamic partition complexes restricted to small confinement zones. (i) Pointillist reconstruction, where each single-molecule event detected is represented by a single green dot. (ii) Single-molecule density plot. Molecules (N) were grouped together using a maximum exploratory radius of 100 nm (d_{Thresh} < 100 nm) and density calculated as N per cell area. The colored scale bar represents the normalized number of detected events per square micrometer. (iii) Temporal localization of single-molecule events. Total imaging time was divided into three color-coded fractions (red, green, and blue represent the first, second, and third fraction of total time, respectively). Single molecules were colored according to the fraction of time in which they were detected and combined in a red, green, and blue additive color model (e.g., yellow represents a spatial zone where independent single molecules were detected in the first and second fractions of imaging time, red + green).

(F) Representative time traces of emission intensity (blue line) for representative ParB$_F$-mEos2 foci. Inset: zoom of the trace forming the main plot in the second timescale.

(G) Histogram of ParB$_F$ confinement zone size distribution. The diameter of each confinement zone was computed from the full-width at half-maximum value, resulting from a two-dimensional Gaussian fitting to the spatial distribution of single-molecule events belonging to a cluster. The frequencies of the confinement zone diameters were plotted with a binning size of 15 nm. The solid gray line represents the fit of a Gaussian distribution to the experimental data (n = 816) with best-fitting parameters values: mean (μ) and SD (σ) = 150 ± 20 nm.

(H and I) (i–iii) ParB$_F$ binding to DNA and *parS*$_F$, which is essential for complex assembly. (i) Pointillist representation of single-molecule events detected by PALM imaging of ParB$_F$-mEos2 variants deficient either in *parS*$_F$ binding (H) or in DNA binding (I) do not form spatial clusters (ii), and ParB$_F$ appears homogeneously distributed in time through the cytoplasm (iii). Color codes are as in (E).

Scale bars represent 500 nm in all images. Orange dotted lines represent cell outlines.

simultaneous multiple detection events or detection of the same ParB$_F$-mEos2 molecule during several consecutive frames (i.e., fluorescence blinking; Annibale et al., 2011a), we analyzed the emission intensity time traces of individual confinement zones. Figure 2F shows that in our PALM imaging conditions, (1) a single emitter per point-spread function is detected at any given time and (2) single events are separated in time for periods longer than the reported fluorescence off-time for mEos2 (inset; t_{off}-mEos2 is ~0.1–0.5 s; Annibale et al., 2011b; Lee et al., 2012). Thus, clusters are not associated with reactivation-induced

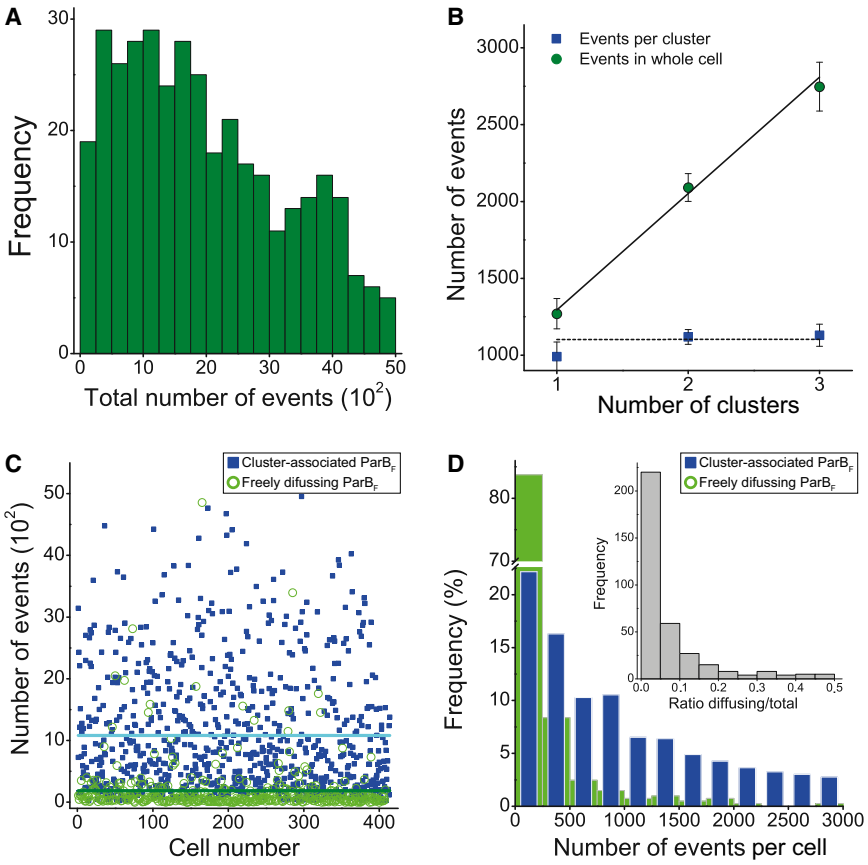

Figure 3. Majority of $ParB_F$ Present in the Cell Is Recruited to the Partition Complexes

(A) Total $ParB_F$ composition per individual cells. The total number of single-molecule events is plotted as a frequency distribution for each detected cell (n = 416).

(B) Total number of $ParB_F$ events per cell (n = 416), which is proportional to the number of clusters. The average number of total events (green dots) and events belonging to clusters (blue squares) are plotted as a function of the number of foci present in the cell. Solid and dashed lines are only guides to the eye. Error bars represent the SEM.

(C and D) $ParB_F$ clusters containing ~90% of the total $ParB_F$ present in the cell. (C) Number of single-molecule events belonging to a cluster (blue solid squares) and freely diffusing (green empty circles) per cell (n = 416). Solid lines represent the mean value of events belonging to clusters (turquoise) and freely diffusing $ParB_F$ (dark green). (D) Frequency distribution (as a percentage) of diffuse (green columns) and cluster-associated (blue columns) $ParB_F$ molecules as a function of the number of events per cell. Inset: frequency plot of the ratio between the freely diffusing and the total number of $ParB_F$ present in each cell.

artifacts of mEos2, and no large under- or overcounting errors of $ParB_F$-mEos2 are introduced (explained later). By analyzing the spatial distribution of individual $ParB_F$ molecules present in each detected cluster ($N_{clusters}$ = 816), we found that the confinement region of $ParB_F$/$parS_F$ complexes has a size of ~150 nm (measured by the full width at half-maximum of the distribution of localizations; Figure 2G). Finally, to discard any clustering artifact due to the presence of the photo-activatable tag (Landgraf et al., 2012), we designed $ParB_F$-mEos2 mutants deficient in DNA-binding activity (triple mutation in the helix-turn-helix [HTH] domain; Ah-Seng et al., 2009) or specifically compromised for $parS_F$ binding (Sanchez et al., 2013). Under imaging conditions identical to those used for wild-type strains, we observed that mutants exhibited a homogeneous cellular distribution in both space and time (Figures 2H, 2I, S2B, and S2C), consistent with $ParB_F$-mEos2 clusters detected by SMLM requiring specific $ParB_F$ interactions with $parS_F$. Detection of rapidly moving $ParB_F$ species—such as $ParB_F$ dimers freely diffusing or interacting rapidly with nsDNA—requires fast acquisition rates; otherwise, image blurring during acquisition can lead to undetected particles, thus biasing the resulting super-resolution image. However, the sub-cellular localization of $ParB_F$ in wild-type or mutant strains was not affected by a considerable reduction in acquisition rate (from 50 to 15 ms), indicating that freely diffusing $ParB_F$ dimers represented a very small proportion of detected localizations. Finally, cells with $ParB_F$ devoid of the mEos2 tag showed barely any detectable single-molecule event under the same imaging conditions (Figure S2D); thus, background fluorescence did not contribute to the detected localizations.

In SMLM, the number of detected single-molecule localization events (N) does not represent the number of absolute proteins, as photo-activatable proteins display stochastic blinking behavior (Deschout et al., 2014) and can exhibit low photo-conversion efficiencies (Durisic et al., 2014), premature photo-bleaching, or partial misfolding. However, N increases with the number of single emitters and can be used to obtain relative measures of the total number of proteins in cells and the proportions of proteins associated or not associated with partition complexes. When analyzing the total number of localization events per cell, we observed a large, heterogeneous distribution reflecting the stochastic behavior of the probe, as well as heterogeneities in the number of foci per cell and in the number of $ParB_F$ molecules per partition complex (Figure 3A). Interestingly, the total average number of localization events per cell was directly proportional to the number of foci per cell (Figure 3B), whereas single $ParB_F$/$parS_F$ complexes contained a constant number of localization events independent of the number of foci per cell. These results reveal that there is probably a minimal number of $ParB_F$ required to form active partition complexes and that $ParB_F$ is redistributed among those complexes as a function of the number of plasmids present in the cell. Next, we determined the proportion of localizations belonging or not belonging to partition complexes. Most $ParB_F$ (~1,100 localizations on average) was contained within the confinement zones defined by the partition complexes, while a minority of $ParB_F$ (~180 localizations) was found outside (Figure 3C). By analyzing the distribution in the number of localizations per cell, we observed that most cells (~85%) contained fewer than 200 localizations outside partition complexes, while

the partition complex displayed more than 500 events in most cells (~60%; Figure 3D). By calculating the ratio between localizations outside and those inside partition complexes, we can estimate the proportion of the cellular pool of $ParB_F$ molecules residing within a partition complex. Most cells showed a ratio below 0.1 (Figure 3D inset), indicating that more than 90% of $ParB_F$ molecules were concentrated within active partition complexes. This analysis combines all cells independent of the number of partition complexes per cell, because no significant differences were observed when cells having one, two, or three partition complexes were analyzed separately (compare Figure 3D with Figure S3). Most of the excess $ParB_F$ molecules are thus trapped close to the centromeres with a $ParB_F$ concentration probably approaching the micromolar-to-millimolar range.

$ParB_F$ Binds Stochastically over a Large Region of Centromere-Flanking DNA

In vivo, $ParB_F$ forms highly confined clusters that localize to defined sub-cellular locations. Importantly, the size and cellular location of these clusters are in part determined by specific interactions with centromere sequences (as explained earlier). To further investigate the architecture and mechanism of the assembly of partition complexes, we turned to chromatin immunoprecipitation sequencing (ChIP-seq) analysis. Specifically, after formaldehyde treatments of F plasmid-carrying cells, DNA was sheared by extensive sonication to provide DNA fragments of ~160 base pairs (bp) on average (Figures S4A and S4B), ensuring that no bias is due to long DNA fragments. After cross-link reversal, DNA reads from high-throughput sequencing were aligned with the genome of reference and enrichment in $ParB_F$-specific immunoprecipitated (IP) DNA was only found on F plasmid (Figures 4A and S4C), not on the *E. coli* chromosome. The maximum of IP DNA reaches 1,700 reads/bp at $parS_F$, well above the intrinsic background level. Strikingly, the ChIP-seq signal drops abruptly at the border of the centromere region, with centromere sequences showing a signal ~2.5-fold larger than neighboring sites (Figure 4A arrows). Then, it decreases gradually over a large region of DNA with $ParB_F$ binding extending over ~5 kb on the left and ~15 kb on the right of $parS_F$. On the left side of $parS_F$, the change occurs near the locus *incC* (represented as a vertical yellow bar in Figure 4A), which corresponds to an array of essential binding sites for the replication initiator RepE (Uga et al., 1999). This suggests that the assembly of a large nucleoprotein complex may perturb, but does not prevent, the ability of $ParB_F$ to propagate over long distances. A similar change in the slope on the right side of $parS_F$ (~25 kb) may correspond to factors bound to a yet-unidentified locus.

To understand the molecular mechanism giving rise to this gradual decrease, we tested the capacity of the two current models (see Introduction) to describe our experimental data. In the filament model, $ParB_F$ spreads uni-dimensionally on DNA from the centromere (Rodionov et al., 1999). This model predicts an exponential decrease with the distance in the ChIP-seq signal (McCoy and Wu, 1973). This prediction is incompatible with the observed experimental behavior over the full range of the genomic coordinates and for physically reasonable parameters (Figures 4A inset, S5B, S5C, and S5G). The spreading and bridging model (Figure S5D; Graham et al., 2014), predicts a ParB-binding profile decreasing linearly from *parS* (Broedersz et al., 2014). This is not observed in our ChIP-seq assay (Figures 4A inset and S5G).

We therefore considered a new model capable of describing our data and previous findings in the literature, with two main properties (Figures S5E and S5F): (1) Starting from microscopy evidence (Figure 2), we assume that $ParB_F$ forms a highly confined focus around *parS*. (2) $ParB_F$ can bind non-specifically to the plasmid DNA inside the focus according to the configuration of the plasmid in space. We expect this configuration to be weakly influenced by $ParB_F$-$ParB_F$ interactions due to the entanglement of the plasmid in the dense environment of the nucleoid. This model, based on stochastic $ParB_F$ binding, predicts that the probability of contact between $ParB_F$, concentrated at the centromere, and DNA sequences, at any distance from $parS_F$, would be determined by the spatial configuration of the DNA, modeled as an ideal (Gaussian) polymer in a dense DNA solution (de Gennes, 1979; Schiessel, 2013). In particular, it is well known that the return to the origin probability of a polymer follows a power law distribution with an exponent of 1.5 (de Gennes, 1979; Schiessel, 2013). Importantly, such a distribution fits the right (over 10.5 kb; coordinates 14.1–24.6) and the left (over 2.1 kb; coordinates 11.3–13.4) sides of our ChIP-seq signal reasonably well (Figures 4A, inset, S5E, and S5G). Thus, this model supports a mechanism in which $ParB_F$ explores the region around the centromere by three-dimensional (3D) stochastic binding. Other curve fittings are not formally excluded (Figure S5), but our model provides the best and simplest explanation for describing the high-resolution data, compared to previous models.

The Assembly of the Partition Complex Requires Synergistic Protein-Protein and Protein-DNA Interactions

To investigate the molecular mechanism by which $ParB_F$ could mediate long-range DNA interactions, we analyzed the formation of $ParB_F$ complexes on large DNA fragments (144 bp) containing only one $ParB_F$-binding site using the electrophoretic mobility shift assay (EMSA; Figure 4Bi). As previously described, $ParB_F$ specifically binds to the 16-bp $parS_F$ sequence with high affinity (2.5 nM; Ah-Seng et al., 2009). At 10 nM $ParB_F$, nearly all the $parS_F$ DNA probe (C144) was shifted to a discrete and specific complex (B1). A second discrete complex (B′2) was detected above 30 nM $ParB_F$ and represented half of the shifted complexes ~500 nM. A third complex (B′3) was also detected above 300 nM. We focused our investigations on the interaction required for the formation of the B′2 complex. Because EMSA was performed in the presence of a large excess of nsDNA, the B′2 complex was not expected to arise from non-specific binding outside the $parS_F$ sites. This was also excluded by (1) comparing the shifted pattern of a $parS_F$ and non-specific probes in the same EMSA gel (Figure S6A), showing that a nsDNA complex (NS1) appeared at a concentration of $ParB_F$ (1 μM) well above the 30 nM needed to detect the B′2 complex, and (2) assaying $ParB_F$ binding to nsDNA by EMSA without an excess of competitor nsDNA (Figure S6B), showing that a complex (NS1) was observed only above 200 nM. From these results, we conclude that the formation of secondary binding complexes requires additional interactions beyond nsDNA binding.

We then performed EMSA with a smaller, 30-bp probe (C30; Figure 4Bv). We found that the formation of B1 complexes is

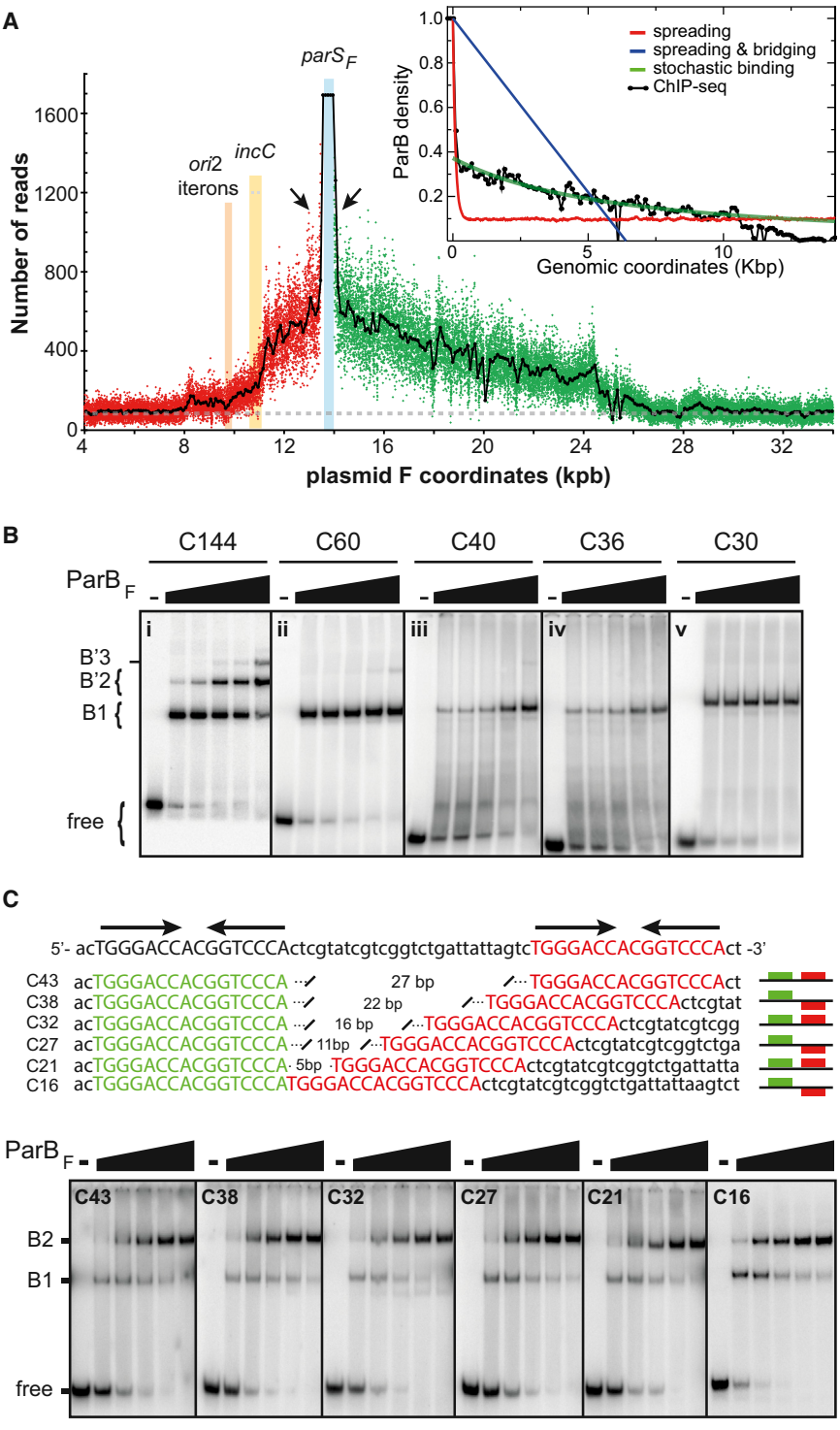

Figure 4. ParB$_F$ Binds Stochastically Outside *parS*$_F$ upon ParB-*parS*, ParB-ParB, and ParB-nsDNA Interactions

(A) High-resolution ChIP-seq of ParB$_F$-binding pattern. Formaldehyde-treated cells carrying F plasmid were immunoprecipitated with anti-ParB$_F$ antibodies. The DNA recovered was quantified by deep sequencing (~50 10^6 reads per library). The number of reads is plotted versus the nucleotide coordinates of pOX38B. For clarity, only the reads between 7 and 34 kb are shown; red and green dots correspond to reads on the left and right sides of *parS*$_F$, respectively. The black line corresponds to the average number of reads per 100-bp windows. The baseline level (90 reads/bp; dashed gray line) was determined by averaging reads per bp on F plasmid with the exclusion of the ParB$_F$-binding zone (7–27 kb). Black arrows indicate the drop in reads on either side of *parS*$_F$. The blue, yellow, and rose vertical boxes represent *parS*$_F$, *ori2* iterons, and *incC* positioning, respectively. See also Figure S4C. Inset: comparison between the ChIP-seq density profile and the different model predictions. The same dataset with binning over 100 bp is shifted to locate *parS* at the origin. The number of reads, plotted in density per site, is displayed only for the right side of *parS* for clarity (black). The predictions of the spreading (red curve; fast decrease from *parS* to an average coverage value), the spreading and bridging (blue curve; linearly decreasing profile), and the stochastic binding (green curve; power law distribution) models are displayed in density per site. See Figure S5 for the definition of these models and the details of the modeling.

(B) Formation of secondary ParB$_F$-DNA complexes, requiring long DNA fragments. EMSA were performed with ^{32}P-labeled DNA fragments of decreasing length carrying a single *parS*$_F$ (Table S1). Reaction mixtures containing 100 μg/ml sonicated salmon sperm DNA were incubated in the absence (–) or the presence of increasing concentrations of ParB$_F$ (black triangle; 0, 10, 30, 100, 300, and 1,000 nM). The position of free and ParB$_F$-bound probes is indicated on the left. B1 represents complexes involving the specific interaction on the 16-bp binding site, while B′2 and B′3 complexes represent secondary complexes involving a *parS*$_F$ site with one or two additional nsDNA-binding interactions, respectively.

(C) DNA spacing variation between two adjacent binding sites, revealing that the ParB$_F$ dimer could bind every 16 bp without steric hindrance. Top: sequences of "Cn" probes, with n corresponding to the number of bp between the first (green) and the second (red) *parS*$_F$ sites. The top sequence corresponds to the consensus sequence between two adjacent *parS*$_F$ sites (inverted arrows). On the right is the schematic position of ParB$_F$-binding sites relative to the face of the double helix. Bottom: EMSA performed as in (B), with B1 and B2 representing complexes involving one or two specific interactions with the 16-bp binding sites, respectively.

as efficient as with C144 probe (Figure 4Bi). However, no secondary B′2 complex was detected even at a high concentration, indicating that a minimum amount of DNA flanking the *parS*$_F$ site is required for the formation of the B′2 complex. It also excludes the possibility, proposed by Schumacher et al. (2010), that each monomer of a ParB$_F$ dimer could contact different DNA molecules. By performing competition experiments with increasing concentration of unlabeled *parS*$_F$-carrying DNA fragments of a

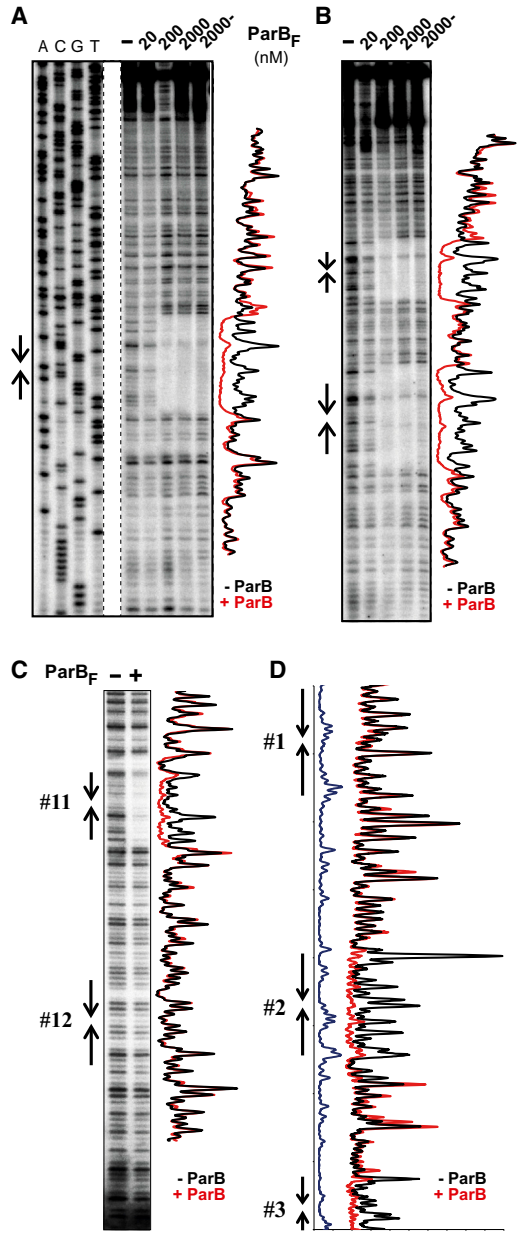

Figure 5. Footprinting Analyses Reveal No Protection Pattern Outside Specific $ParB_F$-Binding Sites

DNase I footprinting assays on DNA probes were performed in vitro (A and B) and in vivo (C and D). Head-to-head arrows correspond to the 16-bp $parS_F$ sites.

(A and B) DNase I footprints on DNA fragments carrying one (A; C144) or two (B; C223) naturally 43-bp spaced $ParB_F$-binding sites. $ParB_F$ concentrations (in nanomolars) are written on top of the gels, and – indicates reactions performed in the absence of competitor DNA. Normalized densitometric scans of gels are shown with black and red lines corresponding to footprints in the absence or the presence of 2,000 nM $ParB_F$, respectively. In (A), the left part corresponds to sequencing reactions of the C144 probe.

(C and D) Exponentially growing cells, induced (+) or not (–) for $parB_F$ expression, subjected to in situ DNase I treatment. Normalized densitometric scans are shown with red, and black lines correspond to $ParB_F$ induced or uninduced. In (D), only the scans are shown. The first and last repeats of the centromere (see Figure S1A) were not protected, indicating that these two slightly degenerated $parS_F$ sites were not bound by $ParB_F$ in vivo.

different size (Figure S6C), we also exclude the possibility that B′2 complexes arise from the assembly of two $ParB_F$ dimers on two DNA molecules.

Next, we investigated the minimal length of the flanking DNA outside the 16-bp $parS_F$ site required for B′2 complex formation, using probes of decreasing lengths with centrally located $parS_F$ sites (Figures 4Bii–4Biv). B′2 complexes were observed with a C60 probe but were barely detectable with C40 and were not detectable with C36, indicating that the minimal length of flanking DNA is 12 bp (Table S1). Interestingly, the DNA with the longest sequence flanking *parS* produced the most B′2 complex, suggesting that the amount of nsDNA close to the $parS_F$-binding site is key for B′2 complex formation.

All together, these results strongly suggest that B′2 complex formation does not result from a unique interaction but rather requires the combination of $ParB_F$-$ParB_F$ (dimer-dimer) and $ParB_F$-DNA interactions.

The Lowest Distance between Two Bound $ParB_F$ Dimers without Steric Hindrance Is 16 bp

$ParB_F$-binding sites are regularly spaced every 43 bp in the centromere sequence, each 16-bp site being separated by 27 bp (Figure S1A). This spacing corresponds to four helical turns of the DNA helix (B form), implying that $ParB_F$ dimers should bind to the same face of the DNA. To determine the closest distance between two sites that support two $ParB_F$ dimers without steric hindrance, we performed EMSA with 63-bp DNA fragments that carry two $ParB_F$-binding sites; the second site was moved by steps of 5 or 6 bp relative to the first site (Figure 4C). With the two $ParB_F$-binding sites naturally spaced by 43 bp (probe C43), we observed two discrete complexes, B1 and B2 (left panel); the former is more abundant at the lowest $ParB_F$ concentrations, while the latter is more abundant at the highest concentrations, as expected. All probes tested displayed this pattern, even when two sites were juxtaposed without separation (probe C16, right panel), and no difference in binding efficiency was observed. Accordingly, an additional $ParB_F$ dimer is able to bind non-specifically between two naturally spaced $parS_F$ sites at $ParB_F$ concentrations. However, this extra binding occurs only at a concentration above 1 μM (Figure S6D). Together, these results clearly reveal that no steric hindrance prevents $ParB_F$ from assembling every 16 bp along DNA.

Partition Complexes Do Not Assemble as Stable Nucleoprotein Complex Outside the Centromere

High-resolution ChIP-seq and subsequent modeling data (described earlier) strongly suggest that $ParB_F$ propagation does not involve 1D spreading on DNA. However, our finding that $ParB_F$ could assemble every 16 bp does not rule out that lateral spreading could stabilize short patches of $ParB_F$ by nearest-neighbor interactions near $parS_F$, as suggested by Graham et al. (2014) and Broedersz et al. (2014). To discriminate between these two possibilities, we measured the DNA sensitivity to cleavage close to $parS_F$ by performing in vitro DNase I footprinting assays (Figures 5A and 5B). As expected, we observed a strong protection on the 16-bp inverted repeat binding sites. However, no protection outside or between the specific binding sites was detected, independent of the presence or absence of

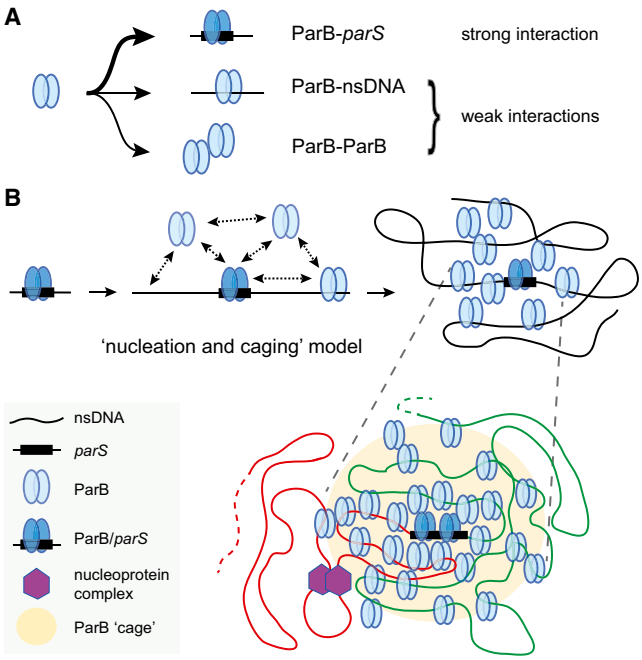

Figure 6. Assembly Mechanism and 3D Architecture of the Partition Complex

(A) ParB protein interactions with its partners. The ParB dimer has a strong affinity for the *parS* DNA site (thick arrow) and weak affinities (thin arrow) for nsDNA and itself.

(B) Nucleation and caging model. The high-affinity *parS* site strongly binds a ParB dimer (left). The transient interactions of ParB with itself and with ParB-nsDNA provide a network of weaker interactions that nucleates the formation of a highly confined ParB zone (middle). By preventing fast ParB diffusion away from the ParB/*parS* complex, these independent but synergistic interactions actively cluster most ParB around *parS* (right). Importantly, the DNA in the vicinity of *parS* would preferentially enter this high-density region of ParB. This results in the stochastic binding of ParB over the centromere-proximal DNA sequences, which depend on the natural loops of the DNA, and leads to the observed power law decrease in ParB density occurring over a large genomic distance. The power-law (dash lines) describes the assembly of the F plasmid partition complex based on the nucleation and caging model. The F centromere is schematically drawn with a black rectangle (only two specific sites are depicted for clarity) to which $ParB_F$ dimers bind with high affinity. Additional ParB dimers are attracted to the vicinity of ParB/*parS* by the network of ParB interactions. The green and red lines represent the DNA adjacent to *parS* on the right and left sides, respectively. The assembly of nucleoprotein complexes, such as paired RepE/iteron complexes (purple hexagons) on the left side of $parS_F$ may reduce the spatial proximity of the surrounding DNA regions from the partition complex. Such an effect, by decreasing the probability that these DNA regions stochastically contact the centromere DNA, may explain the asymmetric distribution of ParB binding on both centromere sides.

competitor DNA, indicating that $ParB_F$-binding adjacent to $parS_F$ is too dynamic to be detected by in vitro DNase I footprinting.

We have shown that more than 90% of $ParB_F$ is clustered in vivo (Figure 2), giving rise to very high local concentrations (>100 μM) that could be involved in the stabilization of lateral spreading. To test this possibility, we investigated the DNA protection near $parS_F$ by performing in situ footprinting assays (Figures 5C and 5D). Although we readily observed $ParB_F$-specific protection on consensus $parS_F$ repeats, no evidence for an altered pattern outside $parS_F$ or between these sites was detected, revealing that in vivo $ParB_F$ dimers have also low binding affinity surrounding the centromere sites. These results strongly suggest that $ParB_F$ binding is not stabilized by nearest-neighbor interactions (1D polymerization) with strongly bound $ParB_F$ on $parS_F$-specific sites and question the formation of small patches of $ParB_F$ along DNA by lateral interactions.

DISCUSSION

Here, we used a highly complementary set of in vivo and in vitro approaches that collectively allowed us to unravel the in vivo assembly mechanism of an archetypical bacterial partition system. Single-molecule super-resolution microscopy on live cells allowed for the precise estimation of the sub-cellular localization and composition of ParB complexes and provided an upper bound for their physical size. To obtain genomic specificity of localization of ParB within partition complexes, we used genome-wide approaches. Uniquely, the specificity and accuracy of this method allowed us to directly test different models for the partition complex assembly using mathematical modeling. Finally, we revealed the interaction network responsible for the mechanism of assembly of these complexes by biochemical methods.

ParB Propagates from the Centromere by Stochastic Binding: The Nucleation and Caging Model

The two most prominent models for the mechanism of binding of ParB to centromere regions (see Figure 1) require ParB to spread uni-dimensionally away from *parS* by forming nucleofilaments along DNA (Broedersz et al., 2014; Graham et al., 2014; Murray et al., 2006; Rodionov et al., 1999). Our data and other published observations are not in agreement with these models (for additional discussion of our detailed arguments, refer to Supplemental Experimental Procedures). Rather, our observations support a conceptually new and simpler molecular mechanism for partition complex assembly that we term the nucleation and caging model. In this model, the centromere acts as a protein nucleation center, while synergistic protein-protein and protein-DNA interactions are responsible for spatially entrapping ParB around *parS* sites (Figures 6B, S5E, and S5F). The key sequential elements of our model are as follows.

(1) ParB dimers bind with high affinity (in the nanomolar range; Ah-Seng et al., 2009; Funnell, 1991) to a limited number of *parS* sites, acting as a strictly required nucleation center that attracts the large majority of the cellular pool of ParB (>90%; Figure 2).

(2) Interactions of ParB dimers with nsDNA and other ParB dimers lead to the 3D entrapment of ParB around *parS* sites. ParBs from F plasmid, as well as from other systems, are able to interact with nsDNA at low affinities (in the sub-micromolar range; Figures 4B and S6). The formation of secondary $ParB_F$ complexes on nsDNA adjacent to *parS* site, mimicking the propagation of ParB on DNA, requires both ParB-ParB (dimer-dimer) and ParB-nsDNA synergistic interactions (Figures 4B and S6). The length dependency of the nsDNA in the efficiency of forming secondary complexes also clearly argues for the combined involvement of both interactions. Moreover, under

the high local ParB concentrations (>100 μM; Figure 2), low-affinity interactions between different free or bound forms of ParB (depicted in Figure 6A) may occur at very high frequencies. ParB dimers dissociating from these low-affinity sites will be locally entrapped by multiple, low-affinity interactions with nsDNA and other ParB dimers spatially confined around *parS* sites (Figure 6B).

(3) ParB acts as a probe of the local, 3D DNA structure around centromeres. The distribution of $ParB_F$ around *parS* obtained in vivo at high resolution (Figures 4A and S5G) can be fit by a power law, which describes the frequency of a polymer returning to a finite region around the origin (de Gennes, 1979; Schiessel, 2013). Our data and modeling are consistent with the binding pattern of $ParB_F$, resulting directly from the probability of the stochastic $ParB_F$ binding to nsDNA neighboring *parS*, where $ParB_F$ is highly concentrated. Although other models are not excluded, and future work will be required to deeply explore these possibilities, the nucleation and caging model provides the best and simplest explanation for the near-nucleotide resolution ChIP-seq data.

We propose that the high frequency of protein-protein and protein-DNA interactions anchored at the centromere site and the folded polymer conformation of DNA, which provides the lattice for spatially confining ParB around *parS*, leads to a caging effect (Figure 6B). In contrast to the spreading and bridging model, the nucleation and caging model does not require nearest-neighbor interactions to stabilize even small ParB nucleofilaments that would bridge and loop DNA over long distances. In our model, all mutations that disrupt any of the interactions would prevent the formation of clusters, as observed with ParB deficient in (1) *parS*-specific binding ($ParB_F$-R219A; Figure 2H) or (2) DNA binding (triple mutation in the HTH domain; Figure 2I). The behavior of the mutant G77S ($ParB_{Bsu}$), expected to be impaired only in the ParB-ParB (dimer-dimer) interaction (Breier and Grossman, 2007), is also consistent with our model, because in vivo it neither forms clusters nor spreads. ParB-induced DNA condensation as observed with in vitro single-molecule assays (Graham et al., 2014; Taylor et al., 2015) could occur but is not required by our model. Diffusion of proteins along the DNA contour (1D sliding) was shown to be limited to ~40–100 bp (Halford and Marko, 2004; Hammar et al., 2012). This sliding length corresponds to the resolution of our ChIP-seq data and is considerably smaller than the spread of the ChIP-seq signal observed around *parS* sites (>10 kb). Thus, we do not expect 1D sliding to have a significant effect on our modeling.

Interestingly, the ParB density profile extends to different lengths on the right and left sides of $parS_F$. On the left side of the centromere, the profile changes near two iteron loci (*incC* and *ori2*; Figure 4), onto which large nucleoprotein complexes assemble and pair together upon binding of the replication initiator RepE (Das and Chattoraj, 2004; Uga et al., 1999). Similar RepA/iterons complexes on plasmid P1 were proposed to act as a roadblock for $ParB_{P1}$ propagation (Rodionov et al., 1999). Our high-resolution ChIP-seq analysis of the $ParB_F$-binding pattern beyond these iteron regions indicates that RepE/iteron complexes do not act as physical barriers but do disturb the long-distance distribution of $ParB_F$ (Figure 4A inset). The nucleation and caging model provides a reasonable explanation for this phenomenon: formation of large and stable nucleoprotein complexes may affect the local DNA organization, which would reduce the spatial proximity between $parS_F$ and sequences beyond the complexes (Figure 6B zoomed in), thus decreasing the probability that $ParB_F$ binds these DNA sequences.

Mechanistic Implication of the Nucleation and Caging Model

Concentrating ParB only at centromeres is essential for the partition process. In the nucleation and caging model, the distribution of ParB molecules in the vicinity of centromeres arises from broadly conserved properties of the ParB family: *parS*-specific binding, nsDNA binding, and dimer-dimer interactions. Our nucleation and caging model, relying on these dynamic and non-specific interactions between macromolecules that promote the active confinement of ParBs, proposes an universally conserved assembly mechanism capable of acting on the various type I *parS* sites existing in nature and allowing cognate ParAs to position and segregate centromere regions independently of *parS* sequences and organization (Hayes and Barillà, 2006). It also explains why cells can segregate plasmids accurately, despite fluctuations in the plasmid copy number: ParB is expressed in vast excess, and the number of ParB molecules per *parS* cluster equilibrates rapidly.

More importantly, our model suggests that ParA is exposed to a very high local concentration of ParB without (1) requiring centromeric sequences extending over large genomic distances and (2) isolating the adjacent DNA into a well-ordered structure that would prevent its accessibility to other processes or interactions. Such a dynamic architecture may have been proved evolutionarily advantageous, because it eliminates physical and topological constraints that would otherwise arise in the origin of replication region where these partition systems are located.

The nucleation and caging model also suggests that our mechanistic understanding of how the most represented type of bacterial partition complexes faithfully segregates is fundamentally incomplete. Type II and III partition mechanisms rely on pushing well-ordered helical protein-DNA filaments with actin- or tubulin-like polymers, respectively (Aylett and Löwe, 2012). In stark contrast, our model of the type I partition system suggests that cytoskeletal ParA ATPases interact with a nucleoprotein complex that is dynamic and not well ordered. It will be interesting to understand how force and directed movement are generated in such a system.

EXPERIMENTAL PROCEDURES

Bacterial Strains, Plasmids, and Growth Conditions

Strains, plasmids and growth conditions are described in Supplemental Information. For microscopy assay, cultures were grown at 30°C with aeration in a supplemented M9 minimal medium (MGC; see Supplemental Information).

Photo-Activated Localization and Epi-Fluorescence Microscopy

Conventional microscopy and PALM imaging were performed as previously described (Cattoni et al., 2013; Fiche et al., 2013). Single-molecule localizations were obtained by using MTT (Sergé et al., 2008). Bacterial contours, localization coordinates, automatic cell classification, and analysis of the

distribution of localization events to detect and classify $ParB_F$ clusters were processed using PALMcbs (Fiche et al., 2013). Size, number of events, and cellular localization were calculated for each cluster. For details, see Supplemental Information.

ChIP Procedure

The ChIP procedure was adapted from (Cho et al., 2011) with some modifications; see Supplemental Information.

ChIP-Seq Analysis and Fit Procedure

A library of precipitated DNA from ChIP preparation was constructed by adding 130-bp DNA adapters and sequenced with Illumina technology. The resulting sequences (~50 10^6 reads per library) were aligned on pOX38B and *E. coli* MG1655 genomes. Each dot plotted on the resulting graphs corresponds to the first nucleotide of each DNA fragment aligned on the entire genome.

Fit Procedure in ChIP-Seq Data Analysis

To fit the curves of $ParB_F$ binding measured by ChIP-seq, we plotted the number of average reads per 100-bp windows versus the coordinates of pOX38B either in a log-log or in a log-linear scale. We then performed a statistical analysis (program Gnuplot) using the ordinary least-squares method (Figure S5).

EMSA

Experiments were performed as described (Bouet et al., 2007) in the presence of sonicated salmon sperm DNA as a competitor (100 μg/ml), using 0.3–1 nM radiolabeled DNA probes generated by PCR or by annealing PAGE-purified oligonucleotides. Proteins were purified as previously described (Ah-Seng et al., 2009).

Footprint Assays

In vitro DNase I footprinting was performed using 10 nM ^{32}P-labeled DNA, and in situ DNase I footprinting was performed as previously described (Bouet and Lane, 2009); see Supplemental Information.

ACCESSION NUMBERS

The accession number for the raw ChIP-seq data reported in this paper is GEO: GSE67869.

SUPPLEMENTAL INFORMATION

Supplemental Information includes Supplemental Experimental Procedures, six figures, and two tables and can be found with this article online at http://dx.doi.org/10.1016/j.cels.2015.07.013.

ACKNOWLEDGMENTS

We thank S. Depaul and I. Canal for technical assistance; N. Campo and S. Queille for helpful advice on fluorescence microscopy and qPCR, respectively; and A. Wright for providing pOX38B. This work has benefited from the facilities and expertise of the high-throughput sequencing platform of I2BC (Gif/Yvette, France). We are grateful to J. Dorignac, F. Geniet, V. Lorman, and J. Palmeri for valuable discussions concerning the theoretical model; M. Baiesi and E. Carlon for fruitful discussions; and F. Cornet, C. Johnson, and J. Palmeri for critical reading of the manuscript. This work was supported by the Agence National pour la Recherche (2010-BLAN-1316 01 and ANR-14-CE09-0025-01). A.S. was supported by a PhD grant from Ministère de la Recherche et de l'Enseignement and by the Fondation pour la Recherche Médicale (FDT20130928025). J.C.W. and A.P. were supported by the Labex NUMEV and by the Scientific Council of University Montpellier 2. Funding for the microscope was provided by FEDER and by the Association pour la Recherche sur le Cancer. S.M.L.M. experiments were performed at the biophysics facility of the Centre de Biochimie Structurale, funded by the France-BioImaging infrastructure and supported by the French National Research Agency (ANR-10-INSB-04).

Received: April 3, 2015
Revised: June 15, 2015
Accepted: July 30, 2015
Published: August 26, 2015

REFERENCES

Adachi, S., Hori, K., and Hiraga, S. (2006). Subcellular positioning of F plasmid mediated by dynamic localization of SopA and SopB. J. Mol. Biol. *356*, 850–863.

Ah-Seng, Y., Lopez, F., Pasta, F., Lane, D., and Bouet, J.Y. (2009). Dual role of DNA in regulating ATP hydrolysis by the SopA partition protein. J. Biol. Chem. *284*, 30067–30075.

Annibale, P., Vanni, S., Scarselli, M., Rothlisberger, U., and Radenovic, A. (2011a). Identification of clustering artifacts in photoactivated localization microscopy. Nat. Methods *8*, 527–528.

Annibale, P., Vanni, S., Scarselli, M., Rothlisberger, U., and Radenovic, A. (2011b). Quantitative photo activated localization microscopy: unraveling the effects of photoblinking. PLoS ONE *6*, e22678.

Aylett, C.H., and Löwe, J. (2012). Superstructure of the centromeric complex of TubZRC plasmid partitioning systems. Proc. Natl. Acad. Sci. USA *109*, 16522–16527.

Betzig, E., Patterson, G.H., Sougrat, R., Lindwasser, O.W., Olenych, S., Bonifacino, J.S., Davidson, M.W., Lippincott-Schwartz, J., and Hess, H.F. (2006). Imaging intracellular fluorescent proteins at nanometer resolution. Science *313*, 1642–1645.

Biek, D.P., and Shi, J. (1994). A single 43-bp *sopC* repeat of plasmid mini-F is sufficient to allow assembly of a functional nucleoprotein partition complex. Proc. Natl. Acad. Sci. USA *91*, 8027–8031.

Bouet, J.Y., and Funnell, B.E. (1999). P1 ParA interacts with the P1 partition complex at *parS* and an ATP-ADP switch controls ParA activities. EMBO J. *18*, 1415–1424.

Bouet, J.Y., and Lane, D. (2009). Molecular basis of the supercoil deficit induced by the mini-F plasmid partition complex. J. Biol. Chem. *284*, 165–173.

Bouet, J.Y., Surtees, J.A., and Funnell, B.E. (2000). Stoichiometry of P1 plasmid partition complexes. J. Biol. Chem. *275*, 8213–8219.

Bouet, J.Y., Rech, J., Egloff, S., Biek, D.P., and Lane, D. (2005). Probing plasmid partition with centromere-based incompatibility. Mol. Microbiol. *55*, 511–525.

Bouet, J.Y., Ah-Seng, Y., Benmeradi, N., and Lane, D. (2007). Polymerization of SopA partition ATPase: regulation by DNA binding and SopB. Mol. Microbiol. *63*, 468–481.

Breier, A.M., and Grossman, A.D. (2007). Whole-genome analysis of the chromosome partitioning and sporulation protein Spo0J (ParB) reveals spreading and origin-distal sites on the *Bacillus subtilis* chromosome. Mol. Microbiol. *64*, 703–718.

Broedersz, C.P., Wang, X., Meir, Y., Loparo, J.J., Rudner, D.Z., and Wingreen, N.S. (2014). Condensation and localization of the partitioning protein ParB on the bacterial chromosome. Proc. Natl. Acad. Sci. USA *111*, 8809–8814.

Cattoni, D.I., Fiche, J.B., Valeri, A., Mignot, T., and Nöllmann, M. (2013). Super-resolution imaging of bacteria in a microfluidics device. PLoS ONE *8*, e76268.

Cho, H., McManus, H.R., Dove, S.L., and Bernhardt, T.G. (2011). Nucleoid occlusion factor SlmA is a DNA-activated FtsZ polymerization antagonist. Proc. Natl. Acad. Sci. USA *108*, 3773–3778.

Das, N., and Chattoraj, D.K. (2004). Origin pairing ('handcuffing') and unpairing in the control of P1 plasmid replication. Mol. Microbiol. *54*, 836–849.

de Gennes, P.G. (1979). Scaling Concept in Polymer Physics (Ithaca, New York: Cornell University Press).

Deschout, H., Shivanandan, A., Annibale, P., Scarselli, M., and Radenovic, A. (2014). Progress in quantitative single-molecule localization microscopy. Histochem. Cell Biol. *142*, 5–17.

Durisic, N., Laparra-Cuervo, L., Sandoval-Álvarez, A., Borbely, J.S., and Lakadamyali, M. (2014). Single-molecule evaluation of fluorescent protein

photoactivation efficiency using an in vivo nanotemplate. Nat. Methods *11*, 156–162.

Erdmann, N., Petroff, T., and Funnell, B.E. (1999). Intracellular localization of P1 ParB protein depends on ParA and *parS*. Proc. Natl. Acad. Sci. USA *96*, 14905–14910.

Fiche, J.B., Cattoni, D.I., Diekmann, N., Langerak, J.M., Clerte, C., Royer, C.A., Margeat, E., Doan, T., and Nöllmann, M. (2013). Recruitment, assembly, and molecular architecture of the SpoIIIE DNA pump revealed by superresolution microscopy. PLoS Biol. *11*, e1001557.

Funnell, B.E. (1991). The P1 plasmid partition complex at *parS*. The influence of *Escherichia coli* integration host factor and of substrate topology. J. Biol. Chem. *266*, 14328–14337.

Graham, T.G., Wang, X., Song, D., Etson, C.M., van Oijen, A.M., Rudner, D.Z., and Loparo, J.J. (2014). ParB spreading requires DNA bridging. Genes Dev. *28*, 1228–1238.

Halford, S.E., and Marko, J.F. (2004). How do site-specific DNA-binding proteins find their targets? Nucleic Acids Res. *32*, 3040–3052.

Hammar, P., Leroy, P., Mahmutovic, A., Marklund, E.G., Berg, O.G., and Elf, J. (2012). The *lac* repressor displays facilitated diffusion in living cells. Science *336*, 1595–1598.

Hayes, F., and Barillà, D. (2006). The bacterial segrosome: a dynamic nucleoprotein machine for DNA trafficking and segregation. Nat. Rev. Microbiol. *4*, 133–143.

Hess, S.T., Girirajan, T.P., and Mason, M.D. (2006). Ultra-high resolution imaging by fluorescence photoactivation localization microscopy. Biophys. J. *91*, 4258–4272.

Landgraf, D., Okumus, B., Chien, P., Baker, T.A., and Paulsson, J. (2012). Segregation of molecules at cell division reveals native protein localization. Nat. Methods *9*, 480–482.

Lee, S.H., Shin, J.Y., Lee, A., and Bustamante, C. (2012). Counting single photoactivatable fluorescent molecules by photoactivated localization microscopy (PALM). Proc. Natl. Acad. Sci. USA *109*, 17436–17441.

Lin, D.C.H., and Grossman, A.D. (1998). Identification and characterization of a bacterial chromosome partitioning site. Cell *92*, 675–685.

Lynch, A.S., and Wang, J.C. (1995). SopB protein-mediated silencing of genes linked to the *sopC* locus of *Escherichia coli* F plasmid. Proc. Natl. Acad. Sci. USA *92*, 1896–1900.

McCoy, B.M., and Wu, T.T. (1973). The Two-Dimensional Ising Model (Cambridge: Harvard University Press), p. 22.

Møller-Jensen, J., Ringgaard, S., Mercogliano, C.P., Gerdes, K., and Löwe, J. (2007). Structural analysis of the ParR/parC plasmid partition complex. EMBO J. *26*, 4413–4422.

Murray, H., Ferreira, H., and Errington, J. (2006). The bacterial chromosome segregation protein Spo0J spreads along DNA from *parS* nucleation sites. Mol. Microbiol. *61*, 1352–1361.

Pillet, F., Sanchez, A., Lane, D., Anton Leberre, V., and Bouet, J.Y. (2011). Centromere binding specificity in assembly of the F plasmid partition complex. Nucleic Acids Res. *39*, 7477–7486.

Rodionov, O., Lobocka, M., and Yarmolinsky, M. (1999). Silencing of genes flanking the P1 plasmid centromere. Science *283*, 546–549.

Rust, M.J., Bates, M., and Zhuang, X. (2006). Sub-diffraction-limit imaging by stochastic optical reconstruction microscopy (STORM). Nat. Methods *3*, 793–795.

Salje, J. (2010). Plasmid segregation: how to survive as an extra piece of DNA. Crit. Rev. Biochem. Mol. Biol. *45*, 296–317.

Salje, J., and Löwe, J. (2008). Bacterial actin: architecture of the ParMRC plasmid DNA partitioning complex. EMBO J. *27*, 2230–2238.

Sanchez, A., Rech, J., Gasc, C., and Bouet, J.Y. (2013). Insight into centromere-binding properties of ParB proteins: a secondary binding motif is essential for bacterial genome maintenance. Nucleic Acids Res. *41*, 3094–3103.

Schiessel, H. (2013). Biophysics for Beginners: A Journey through the Cell Nucleus (Pan Stanford Publishing).

Schumacher, M.A., and Funnell, B.E. (2005). Structures of ParB bound to DNA reveal mechanism of partition complex formation. Nature *438*, 516–519.

Schumacher, M.A., Glover, T.C., Brzoska, A.J., Jensen, S.O., Dunham, T.D., Skurray, R.A., and Firth, N. (2007). Segrosome structure revealed by a complex of ParR with centromere DNA. Nature *450*, 1268–1271.

Schumacher, M.A., Piro, K.M., and Xu, W. (2010). Insight into F plasmid DNA segregation revealed by structures of SopB and SopB-DNA complexes. Nucleic Acids Res. *38*, 4514–4526.

Sergé, A., Bertaux, N., Rigneault, H., and Marguet, D. (2008). Dynamic multiple-target tracing to probe spatiotemporal cartography of cell membranes. Nat. Methods *5*, 687–694.

Surtees, J.A., and Funnell, B.E. (1999). P1 ParB domain structure includes two independent multimerization domains. J. Bacteriol. *181*, 5898–5908.

Taylor, J.A., Pastrana, C.L., Butterer, A., Pernstich, C., Gwynn, E.J., Sobott, F., Moreno-Herrero, F., and Dillingham, M.S. (2015). Specific and non-specific interactions of ParB with DNA: implications for chromosome segregation. Nucleic Acids Res. *43*, 719–731.

Uga, H., Matsunaga, F., and Wada, C. (1999). Regulation of DNA replication by iterons: an interaction between the *ori2* and *incC* regions mediated by RepE-bound iterons inhibits DNA replication of mini-F plasmid in *Escherichia coli*. EMBO J. *18*, 3856–3867.

Vecchiarelli, A.G., Mizuuchi, K., and Funnell, B.E. (2012). Surfing biological surfaces: exploiting the nucleoid for partition and transport in bacteria. Mol. Microbiol. *86*, 513–523.